Arabian Journal for Science and Engineering
https://doi.org/10.1007/s13369-026-11290-2

RESEARCH ARTICLE-COMPUTER ENGINEERING AND COMPUTER SCIENCE

Evaluation of Peripheral Arterial Disease Through Thermal Imaging and Machine Learning: A Texture- and Frequency-Based Approach

H. Feza Carlak[1] · Salih Ozcobanoglu[2] · Yakup Irim[3,4]

Received: 22 September 2025 / Accepted: 1 April 2026
© The Author(s) 2026

Abstract

Peripheral arterial disease (PAD) is a common cardiovascular condition. The aim of this study is to facilitate the early diagnosis of PAD in the lower limbs and to develop a non-invasive assistant medical diagnostic method to monitor the treatment process. The proposed method was developed using a combination of thermal imaging, image processing, and artificial intelligence algorithms. The proposed framework was evaluated on a cohort of 40 participants divided into four groups: athlete, healthy, individuals at cardiovascular risk, and patients with PAD. Infrared thermal images of the lower extremities were acquired under standardized conditions before and after a controlled physical effort protocol. Haralick texture features, including energy, contrast, correlation, homogeneity, and entropy were calculated. Hot region distribution images were generated using K-means clustering. Frequency components value of any signal was calculated by wavelet transform. The highest temperature increase due to effort was observed in the athlete group ($\Delta T = 0.96$ °C), while the lowest was observed in the patient group ($\Delta T = 0.38$ °C). The Kruskal–Wallis H test results showed statistically significant differences in contrast ($p = 0.017$) and homogeneity ($p = 0.028$) between groups. The Haralick texture features were trained using the Support Vector Machine algorithm, achieving a 95.7% success rate. Hot region images were trained using a convolutional neural network model, which also achieved a 95.7% success rate. Frequency features were trained using the K-Nearest Neighbors algorithm, achieving an 83.3% success rate. Subsequently, an eXtreme Gradient Boosting (XGB) model achieved a success rate of 92.9%. The technology explored in this study holds potential as an assistant method for detecting, monitoring, and evaluating responses to treatments for conditions such as peripheral atherosclerotic diseases, diabetic vascular diseases, and others.

Keywords Thermal Imaging · Peripheral arterial disease · Image processing · XGB model · Convolutional neural network

1 Introduction

PAD is a common cardiovascular condition characterized by arterial stenosis, which reduces blood flow, particularly to the lower extremities [1]. Despite its prevalence, it is estimated that the majority of individuals with PAD are estimated to remain undiagnosed and untreated [2]. The most common symptom of PAD is pain in the legs during physical activity or at rest [3]. This discomfort arises due to insufficient oxygen delivery to tissues during exercise, leading to pain in affected individuals [4]. Major risk factors for developing PAD include age, tobacco use, body mass index (BMI), hypertension, and diabetes [5].

The early diagnosis and management of the treatment process in PAD are critical for reducing mortality and morbidity rates. However, because the PAD is often asymptomatic, individuals typically do not seek medical support and are not screened by clinicians without a confirmed diagnosis. Given the challenges in diagnosing PAD at an early stage, the development of non-invasive diagnostic tools is of significant importance [6]. While invasive assessment methods offer high accuracy, they are often costly and inconvenient for patients [7]. In contrast, non-invasive methods have the potential to be more widely adopted for early diagnosis and monitoring of treatment.

✉ Yakup Irim
yirim@sinop.edu.tr

[1] Department of Electrical-Electronics Engineering, Faculty of Engineering, Akdeniz University, Antalya, Turkey

[2] Department of Cardiovascular Surgery, Faculty of Medicine, Akdeniz University, Antalya, Turkey

[3] Department of Electrical-Electronics Engineering, Institute of Natural Sciences, Akdeniz University, Antalya, Turkey

[4] Department of Electronics and Automation, Vocational High School, Sinop University, Sinop, Turkey

Published online: 15 April 2026

Diagnosing PAD is crucial to prevent adverse outcomes such as pain during physical activity, resting pain, and limb or tissue loss [8]. Catheter-based X-ray angiography is widely recognized as the gold standard for assessing the severity and location of PAD in patients. However, this method carries risks due to its invasive nature and the use of contrast material and ionizing radiation, which can be harmful to the kidneys [9, 10]. Several non-invasive alternatives, including computed tomography angiography (CTA), magnetic resonance angiography (MRA), color duplex ultrasound (CDU), and color duplex imaging (CDI), are available for PAD evaluation [11–15]. Despite their utility, these methods have notable drawbacks, such as high costs and potential health risks. In contrast, thermal imaging offers significant advantages as a non-invasive, relatively low-cost diagnostic tool that poses no threat to human health.

Since the metabolic heat generation and thermal properties of tissue vary depending on the type and health condition of the tissue, thermal infrared imaging has potential applications in the diagnosis, treatment, and follow-up stages in clinical settings [16]. Thermal imaging is a high-resolution and risk-free system that does not emit harmful radiation, unlike tomography and X-ray imaging technologies. It is also non-invasive, comfortable for patients, painless, and offers high sensitivity with acceptable diagnostic accuracy. Furthermore, it is a fast, real-time imaging method that records the thermal radiation emitted from skin surfaces, displaying temperature distribution images of body tissues in real-time. These characteristics make it suitable for long-term and repetitive use. Given these advantages, infrared thermal imaging serves as an alternative or complementary tool to other imaging modalities in clinical applications [17, 18].

Several studies have evaluated peripheral vascular structures in the lower extremities using thermal imaging. In studies conducted without applying any image or signal processing to the thermal images of individuals diagnosed with disease through clinical tests, Subramaniam et al. [19] showed that patients exhibit abnormal temperature distributions in their thermal images. Staffa et al. [20] found a high correlation between the ankle–brachial index (ABI) and the temperature distribution observed in thermal images. Wallace et al. [21] confirmed a strong correlation between the thermal ankle–brachial index (tABI) and ABI by calculating tABI from the maximum temperature values in thermal images of the hand and foot areas captured with a smartphone-based thermal camera. Huang et al. [22] working with thermal images, demonstrated that while there is little difference in the temperature distributions of patients and healthy individuals at rest, significant temperature changes were observed after a 6-min walk. Patients showed minimal temperature change, whereas healthy individuals exhibited a substantial temperature variation. This finding supports the effectiveness of thermal imaging in evaluating the peripheral vascular structures of the lower extremities in resting state. Gauci et al. [23] examined temperature distributions on the palms, legs, and soles of diabetic patients and demonstrated that the disease could be diagnosed using this method. Kostadinov [24] highlighted the potential of combining thermal imaging with machine learning for detecting and evaluating PAD, offering a non-invasive, accessible, and cost-effective approach. Sowa et al. [25] explored the use of thermal imaging as an adjunct to other methods like CT, MRA, and angiography in evaluating PAD. Deng et al. [26] investigated thermal imaging as a screening tool for deep vein thrombosis (DVT), showing that pseudocolor analysis of thermal images can aid in DVT detection. To further evaluate the potential of thermal imaging for PAD, Antonio de Carvalho Abreu et al. [27] examined its correlation with the ABI and found a significant relationship between the two methods. In a study by Kleiss et al. [28], hyperspectral and thermal imaging methods were assessed in treating PAD. The results indicated that hyperspectral imaging outperformed thermal imaging on a short-term scale. Zbroja et al. [29] explored the effect of carbon dioxide bathing on peripheral blood circulation in PAD patients, showing that thermal imaging could effectively detect changes in blood flow and body temperature. Zenunaj et al. [30] examined the relationship between thermal imaging, ABI calculation, and duplex scanning in PAD assessment, identifying a strong correlation between thermal imaging and these methods.

Several studies have reported significant differences in temperature distribution patterns between patients clinically diagnosed with PAD and healthy individuals. However, the current literature lacks a standardized and systematic framework for the early detection of PAD or for quantifying the degree of functional vascular impairment. Many existing investigations have primarily focused on resting-state temperature measurements and have not incorporated advanced analytical methodologies such as quantitative image processing or artificial intelligence–based modeling. Consequently, their ability to detect subtle or early stage vascular dysfunction remains limited. This study proposes a diagnostic method that addresses the aforementioned gap by integrating thermal imaging with image processing and artificial intelligence algorithms. This method provides functional insights into the peripheral vascular structures of the lower extremities, thereby contributing to the advancement of early PAD detection.

This study presents an assistant diagnostic framework for the early detection of lower extremity PAD, as well as for treatment monitoring, by integrating thermal imaging with image processing and artificial intelligence techniques. Participants were categorized into four groups: athletes, healthy, at-risk individual, and patients diagnosed with PAD. As a standardized exertion protocol, participants walked at a speed

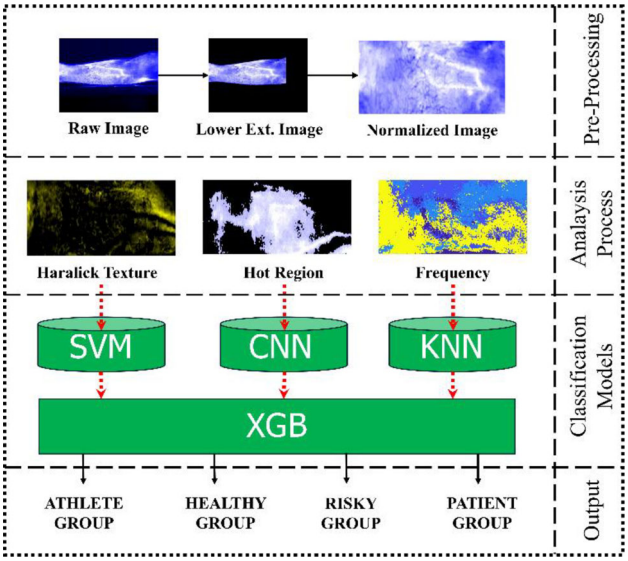


Fig. 1 Flowchart of the system

of 6 km/h for 10 min. Thermal recordings of superficial tissue perfusion in the lower extremities were acquired before and after exercise. Effort-induced temperature distributions and perfusion-related thermal increases were analyzed across groups. The greatest temperature increase was observed in the athlete group, whereas the smallest increase was detected in the patient group. Image processing algorithms were applied to extract quantitative features characterizing spatial temperature distribution. A convolutional neural network (CNN) was trained using post-exercise thermal distribution images. Statistical analysis ($p < \alpha$, $\alpha = 0.05$) of Haralick texture features revealed significant differences in contrast, and homogeneity. These texture features were subsequently classified using a support vector machine (SVM) model. Additionally, frequency domain characteristics derived from post-exercise thermal recordings were analyzed and classified using a k-nearest neighbors (KNN) algorithm. The probabilistic outputs of the three trained models (CNN, SVM, and KNN) were then used as input features for an eXtreme Gradient Boosting (XGB) meta-classifier. The final XGB model achieved an overall classification accuracy of 92.9%. Overall, the findings suggest that the proposed framework may support the non-invasive assessment of vascular dysfunction, reduced vascular compliance associated with fibrosis, and perfusion abnormalities potentially related to plaque formation. A schematic overview of the system architecture is provided in Fig. 1.

2 Methods

2.1 Subjects, Data Acquisitions and Experimental Procedures

A total of 40 participants (local ethics committee approval number: 2012-KAEK-20) were enrolled in the study and equally distributed into four groups ($n = 10$ per group): athlete, healthy, at-risk individuals, and patient. For each participant, thermal images were acquired under pre-effort and post-effort conditions, resulting in two primary thermal datasets per individual. Thermal data were captured using the FLIR T450sc infrared thermal camera. The infrared thermal camera with 320 × 240 resolution was used for thermography of individuals. The camera accuracy is < 2%, the thermal sensitivity (NETD) is < 40 mK, and the factory calibration spectral wavelength is in the range of 7.5–13 μm (long-wave infrared wavelength). It has a geometric resolution of 1.36 mrad and a 25°–19° field of view lens with a minimum focal length of approximately 80 cm. The emissivity is $\varepsilon = 0.98$ for all analyzed regions. The camera is able to record the temperature range of an object from − 20 to + 120 °C. Recording was performed at a frame rate of 30 frames per second (fps). The recording parameters were set to humidity (55%), emissivity (0.98), and ambient temperature (24 °C). Individuals were divided into four groups by taking sports life, body mass index (BMI), tobacco consumption, and family history of vascular disease into account.

Thermal recordings were conducted in a climate-controlled laboratory environment maintained at 24 °C with a relative humidity between 35 and 45%. Prior to image acquisition, participants remained seated in the controlled room for 15 min to allow thermal stabilization and equilibration with ambient conditions. During the measurement procedure, participants wore clothing that exposed the feet to ensure unobstructed thermal assessment.

The infrared thermal camera was calibrated before each recording session to ensure measurement accuracy. Baseline (pre-effort) thermal images were first acquired under resting conditions. Subsequently, participants performed a standardized walking protocol on a treadmill at a constant speed of 6 km/h for 10 min. This fixed duration and intensity were selected to ensure comparable physiological stress across all study groups. Post-effort thermal images were captured immediately after completion of the exercise protocol.

During image acquisition, participants positioned their feet within a custom-designed fixation apparatus to minimize

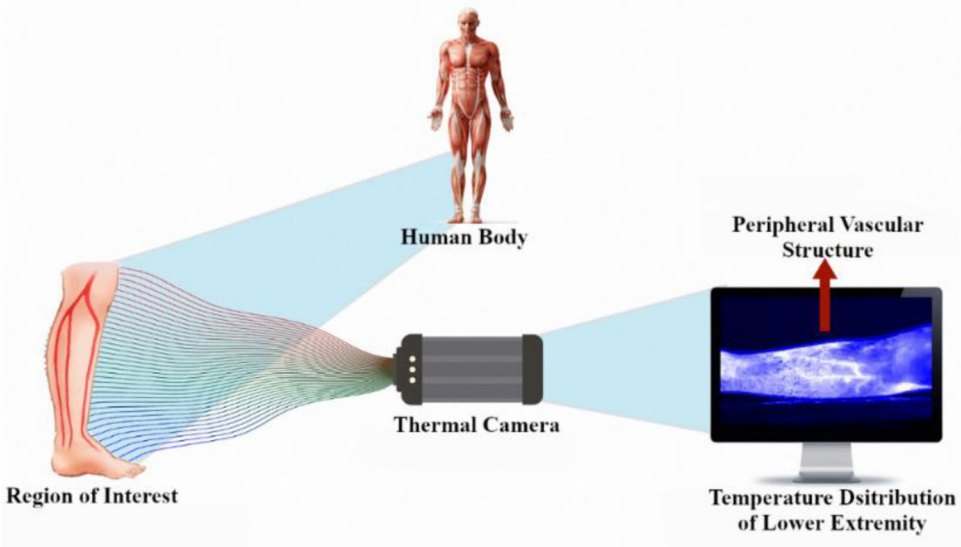


Fig. 2 Block diagram of the assessment of peripheral vascular endothelial function using a thermal imaging system

movement artifacts and ensure consistent spatial alignment across recordings. This setup enabled reproducible and noise-reduced thermal measurements suitable for quantitative analysis. The lower extremity below the knee region is imaged for 60 s from a one-meter distance (Fig. 2).

Participants were categorized into four distinct groups—athletes, healthy, at-risk individuals, and patients with PAD—to represent varying stages of vascular function and physiological adaptation. The athlete group consisted of individuals engaged in regular high-intensity physical training and without known cardiovascular risk factors, serving as a reference for optimal vascular and thermoregulatory performance. Healthy group included participants without diagnosed cardiovascular disease and without major PAD-related risk factors, representing normative physiological conditions. The at-risk group comprised individuals without clinically diagnosed PAD but presenting established cardiovascular risk factors, such as elevated body mass index, smoking history, or a positive family history of vascular disease. This group was intentionally included to explore whether infrared thermal imaging could detect early functional vascular alterations prior to overt clinical manifestation, thereby evaluating the potential of the proposed method as a screening and risk stratification tool. Such individuals may exhibit subtle impairments in endothelial function and microcirculatory regulations that are not yet detectable using conventional diagnostic criteria. The patient group consisted of individuals with clinically confirmed PAD based on standard vascular assessments. The clinical criteria used for group classification are summarized in Table 1.

The inclusion of four distinct groups was deliberately designed to investigate not only overt pathological conditions but also transitional and subclinical stages of vascular dysfunction. This stratified design enabled the evaluation of progressive changes in microcirculatory and thermoregulatory responses under physiological stress, moving beyond a simple binary comparison between healthy and diseased states. By incorporating an at-risk group alongside healthy controls and clinically diagnosed patients, the proposed framework facilitates the exploration of infrared thermal imaging as a potential tool for early functional screening and longitudinal monitoring of PAD-related vascular alterations.

2.2 Pre-processing Stage

Prior to feature extraction, a systematic pre-processing pipeline was applied to all thermal images in order to reduce background noise and standardize the region of interest. After removing background noise from the raw thermal images, a normalization procedure was performed in which the lower extremity region was positioned within a fixed template to ensure spatial consistency across samples.

For segmentation of the lower extremity region, the Snake algorithm [31] was employed. In the initial stage, a boundary enclosing the region of interest (foot area) was defined. This initial contour was iteratively updated by minimizing a combined energy function consisting of internal energy (ensuring contour smoothness and continuity) and external energy (based on image gradient information). The contour evolved toward prominent thermal gradients in the image and converged along the anatomical boundaries of the foot. As a result, the foreground (foot region) was reliably separated from background noise. The movement of the initial boundaries in the direction of the leg region is shown in Fig. 3.

Following convergence of the Snake algorithm, the background was completely removed and a binary mask was generated for each image. The knee region, which was outside the scope of the present study in terms of temperature

Table 1 Clinical criteria used for group assignment

Criterion	Athlete	Healthy	Risky	Patient
BMI (kg/m^2)	< 25	< 25	≥ 30	Any
Smoking history	No	No	≥ 10 years (1 pack per day)	Any
Family history of PAD	No	No	Yes	Any
Hypertension/diabetes	No	No	Possible	Yes
Clinical PAD diagnosis	No	No	No	Yes

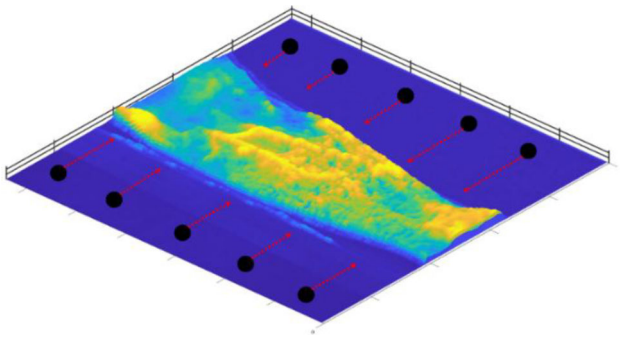


Fig. 3 Moving the initial border points toward the leg area

variation analysis, was manually excluded for all participants to maintain anatomical consistency. All pre-processing steps were applied identically to both pre-effort and post-effort images to ensure methodological consistency and to prevent potential procedural bias.

2.3 Normalization Process

The geometric structure of the lower extremity varies among individuals in terms of size and shape. To ensure spatial consistency across subjects, a normalization procedure was applied by mapping each lower extremity image onto a predefined reference template. Because the anatomical contours of the lower extremity are irregular, normalization was performed by treating each row and column of the image as independent one-dimensional signals and rescaling them to match the template dimensions. During this process, cubic spline interpolation [32] was applied to the one-dimensional signals. In the cubic spline interpolation method, each interval between adjacent data points is approximated using a third-order polynomial, ensuring smooth transitions across the domain. Accordingly, the cubic polynomial defined over the interval $[x_i, x_{i+1}]$ can be expressed as follows:

$$g_i(x) = a_0 + a_1(x - x_i) + a_2(x - x_i)^2 + a_3(x - x_i)^3 \quad (1)$$

Polynomial segments are denoted by $g_i(x)$ and a represents the coefficients.

Cubic spline interpolation was used to normalize the lower extremity temperature distribution image and histogram analysis was performed to verify that the temperature gradients were not distorted. A comparison was made between the temperature histogram of the normalized thermal image and the original thermal image. MATLAB (2022a) software was used for all analysis and image processing. The temperature image of the lower extremity is normalized to a 200 × 400 matrix. The normalization process prevents the noises generated by the superfluous regions during feature extraction. The thermal image obtained by the normalization process is given in Fig. 4.

2.4 Temperature Distribution Analysis

The temperature distribution in the lower extremities serves as an important indicator of the functional status of peripheral vascular structures. High-temperature regions were identified from the normalized lower extremity images. To extract and quantify these regions, the K-means clustering algorithm [33] was applied to the temperature value images, in which each pixel represented its corresponding real temperature value. The images were partitioned into three clusters corresponding to high-temperature (hot), and low-temperature (cold) regions. The K-means algorithm partitions a dataset consisting of n data points into k distinct clusters by minimizing the within-cluster variance. The cluster assignments for the data points are determined as follows:

$$\sum_{j=1}^{K} \sum_{x_i \in S_j} \left\| x_i - \mu_j \right\|^2 \quad (2)$$

where μ_j is an average of the elements in the class, x_i is the elements in the data.

Pixels that have high-temperature close to each other were classified and the structure of temperature distribution were examined, and the images of temperature distributions belonging to athletes, healthy, risky, and patient were evaluated. The regional differences of the hot region distributions of one individual from each group were shown in Fig. 5.

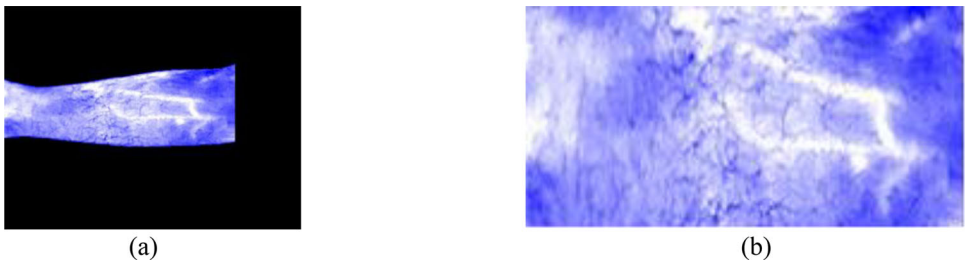


Fig. 4 **a** Temperature image of the lower extremity; **b** Normalized temperature image of the lower extremity

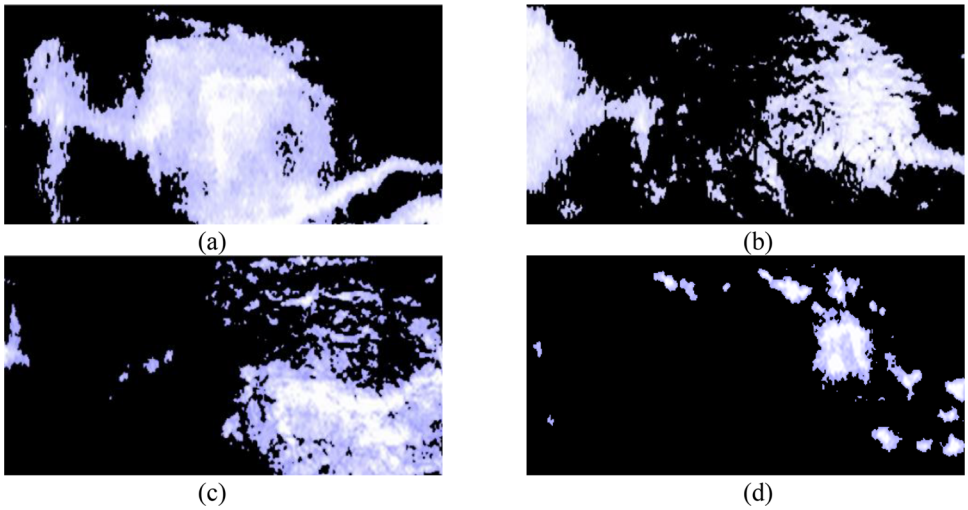


Fig. 5 Temperature distribution images of lower extremity tissue perfusion **a** athletes; **b** healthy; **c** risky; **d** patient people

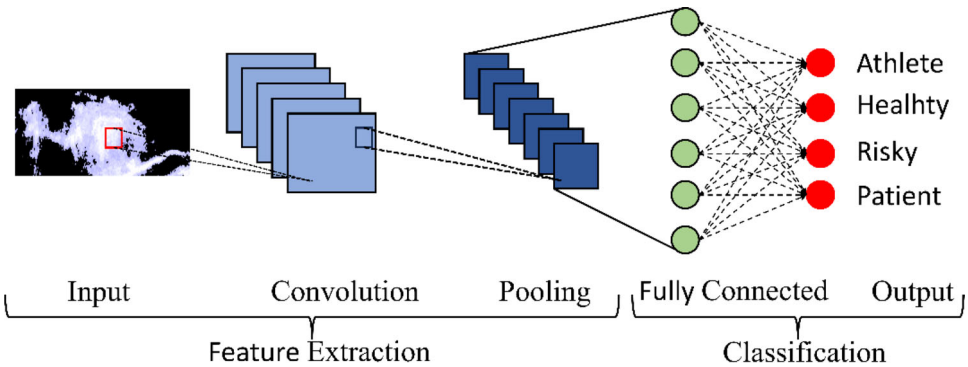


Fig. 6 Structure of the CNN architecture

2.5 Convolutional Neural Network Application

A CNN model was trained to classify groups using temperature distributions of high-temperature image regions [34, 35]. The new CNN model was designed for the proposed imaging system, and 95.7% accuracy was acquired from the temperature distribution images. The general structure of the designed CNN model is given in Fig. 6. The images of temperature distributions are given as an input to the CNN model without extracting the feature from the temperature distribution images and the classification result was obtained in the output of the model.

To ensure a robust and unbiased evaluation of model performance, data partitioning was conducted at the participant level. This strategy prevented images derived from the same individual from appearing across training, validation, and test sets, thereby eliminating the risk of data leakage. The dataset was divided using stratified sampling to preserve class distribution, with 70% allocated to the training set, 15% to the validation set, and 15% to an independent test set.

To mitigate the limitations imposed by the relatively small sample size and to enhance generalizability, 5-fold cross-validation was applied within the training set. Furthermore, data augmentation techniques were applied solely to the training set, while the validation and test sets consisted only of original, non-augmented samples. This structured validation framework was designed to minimize overfitting and to provide a realistic and reliable estimate of model performance under practical deployment conditions.

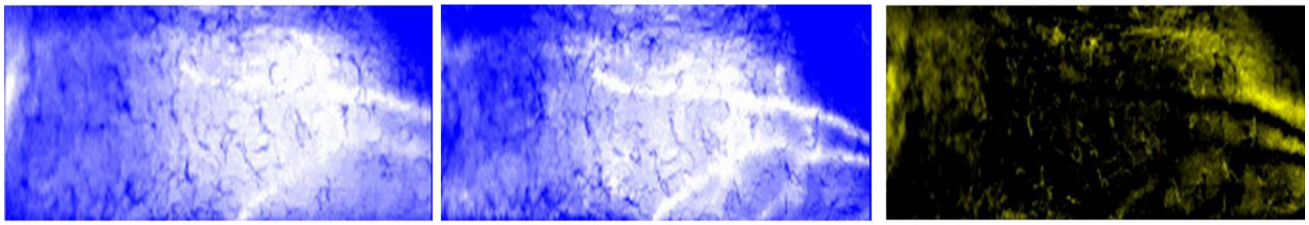


Fig. 7 **a** Normalized thermal images pre-effort; **b** Post-effort; **c** The difference of the normalized thermal images pre and post-effort

2.6 Haralick Texture Features Extraction and Statistical Analysis

The temperature difference images were obtained by taking the difference of the thermal images captured pre and post-effort. The normalized difference thermal image is given in Fig. 7. Haralick texture features were extracted for the detailed assessment of the invisible differences between the images [36]. Five Haralick texture features as energy, contrast, correlation, homogeneity, and entropy were calculated from the temperature variation image using the gray-level co-occurrence matrix (GLCM).

In the statistical analysis, a statistically significant difference $p < \alpha$ between the extracted features among the groups was observed ($\alpha = 0.05$). In statistical hypothesis testing, two hypotheses, "zero hypotheses" (H_0) and "opposite hypothesis" (H_1), were examined [37].

SPSS 18 program was used for the statistical analysis of the findings and the conformity of continuous variables to normal distribution was examined by the Kolmogorov–Smirnov test. In cases where parametric test assumptions are not provided, the nonparametric alternative of this test is Kruskal–Wallis H test. When more than two groups were compared, the Bonferroni correction was used as a post hoc test for pairwise comparisons. Paired comparisons were made using Mann–Whitney U. A 95% significance level (or $\alpha = 0.05$ margin of error) was used to determine the differences in the analyzes.

2.7 Frequency Analysis

Thermal data collected tissue perfusion of lower extremity peripheral vascular structures pre and post-effort for 60 s. Thermal recordings were recorded for 60 s to examine the time-dependent temperature changes of tissue perfusions of individuals. The heat loss frequency of the tissues over the temperature changes on a pixel basis in the lower extremity region was determined.

Each thermal recording contains a total of 1800 frames. Each frame of the thermal recording was extracted in PNG format. For each (i,j) pixel in the image, temperature change signals (1×1800) were obtained depending on time. The

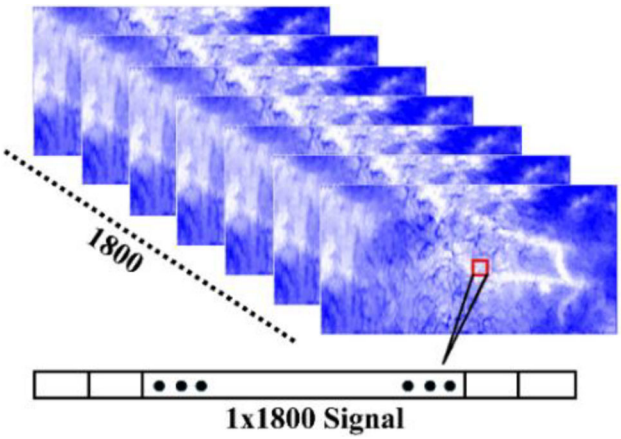


Fig. 8 Generation of a 1D signal for each pixel of the normalized thermal image of the object

frequency components and dominant frequency value of this signal were calculated by wavelet transform [38]. The acquisition of the 1D signals for each pixel of the thermal video data is shown in Fig. 8.

2.8 XGB Model and Data Augmentation

The selection of machine learning models in this study was motivated by the heterogeneous characteristics of thermal imaging data and the need to capture complementary spatial, textural, and frequency domain information reflecting vascular function. CNN was employed to automatically learn complex spatial temperature patterns and hot region distributions directly from thermal images, without reliance on handcrafted feature assumptions. In parallel, texture-based and frequency domain approaches were incorporated to explicitly quantify spatial heterogeneity, perfusion symmetry, and post-exercise thermal recovery dynamics, which are physiologically associated with microcirculatory regulation and vasodilatory responsiveness in peripheral vascular structures.

To integrate these complementary classifiers, an XGB-based ensemble architecture was adopted as a meta-classifier. XGB was selected for its capacity to model nonlinear interactions among correlated probabilistic inputs, its robustness in

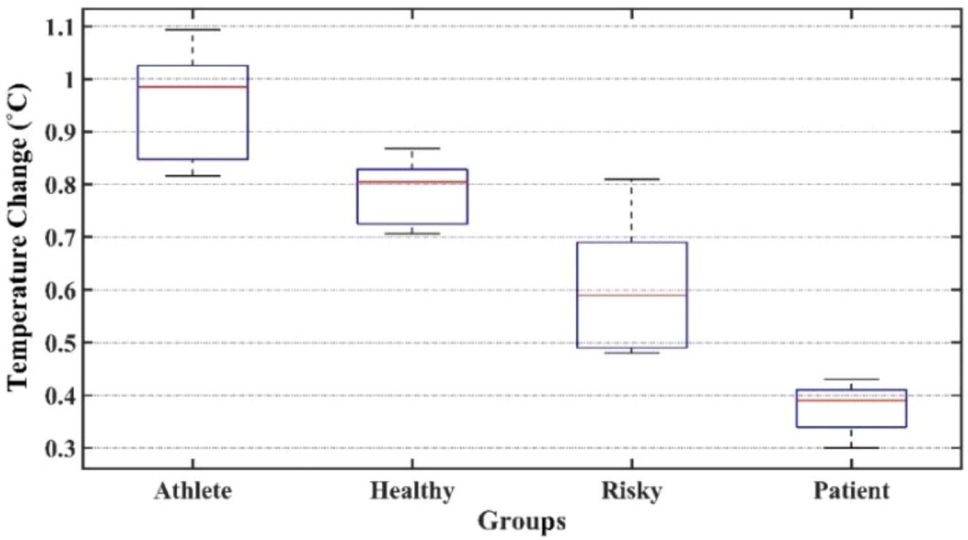


Fig. 9 Mean values of temperature differences of the athlete, healthy, risky and patient. Temperature changes were calculated by taking the difference of thermal images pre and post-effort

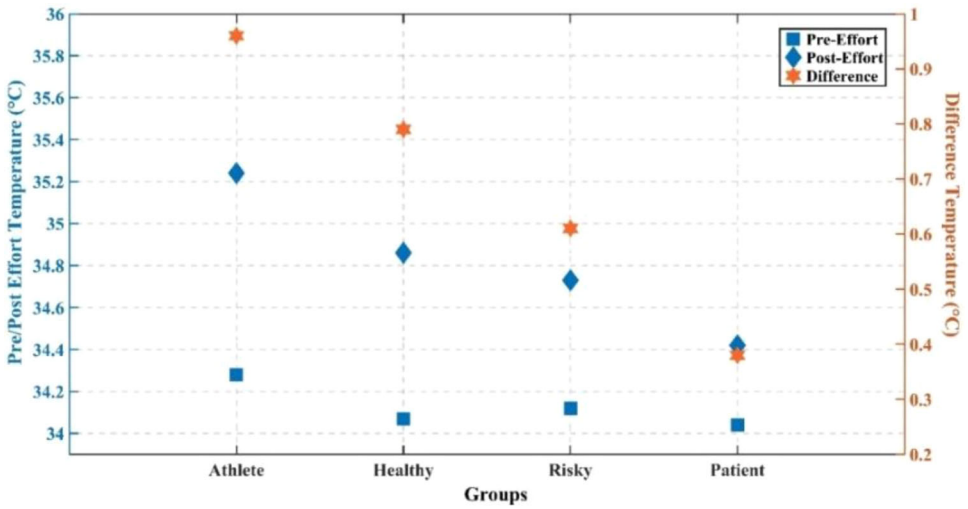


Fig. 10 Mean temperature values of tissue perfusions pre- and post-effort

small-to-moderate sample settings, and its ability to provide gain-based feature importance measures to enhance interpretability. This stacking-based strategy enables the aggregation of strengths from individual models while mitigating the overfitting risk inherent to single-model approaches, thereby improving overall robustness and generalizability.

Given the limited sample size, data augmentation techniques were applied to increase variability within the training dataset and improve model generalization. During preprocessing, background noise and non-relevant anatomical regions were excluded from the lower extremity region of interest (ROI). Specifically, the foot and knee regions were removed due to potential artifacts related to sweating and motion. To ensure an unbiased evaluation, augmentation procedures were applied exclusively to the training set. Furthermore, dataset partitioning was performed at the participant level to prevent data leakage between training, validation, and test sets.

Geometric and photometric approaches are commonly used in data augmentation processes in the literature [39]. Small-scale geometric transformations were used to mimic the strong variations observed in the actual data. These transformations included rotation ($\pm$ 7°), translation along the horizontal and vertical axes ($\leq$ 5%), scaling (0.90–1.10) and slight shear transformations (shear $\leq$ 5°). Reflections of mirror images resulting from geometric transformations were not used because they are not physiologically realistic.

Although cross-validation is commonly employed to estimate model generalization, it was not adopted in this study due to the limited dataset size and the use of data augmentation. In cross-validation settings, augmented samples derived from the same subject may inadvertently appear in both training and validation folds, leading to data dependency and inflated performance metrics. To avoid this issue, a strict participant-based hold-out strategy was preferred. This approach prioritizes data independence and provides a more

conservative and reliable evaluation of model performance under the current experimental constraints.

The XGB meta-classifier was optimized using a grid search strategy. Multiple combinations of hyperparameters—including learning rate (η), maximum tree depth, number of boosting iterations, subsampling ratios, column sampling ratios, and regularization parameters—were systematically evaluated. The configuration yielding the best validation performance was selected for final model training. To promote stable learning and reduce overfitting, shallow trees (maximum depth = 3) and a relatively low learning rate (0.05) were employed. Subsampling and column sampling ratios were set to 0.8 to introduce additional regularization and reduce feature correlation.

In total, twelve probabilistic output coefficients were obtained from the three base models. These coefficients constituted the input layer of the XGB meta-classifier, while the final class prediction was generated at the output layer. The primary advantage of this ensemble approach is its ability to resolve inconsistencies among individual model predictions by learning optimal combinations of their outputs. By training on the probabilistic outputs of the base models, the XGB meta-classifier determines the most reliable final classification in a data-driven manner, thereby improving overall robustness and decision consistency.

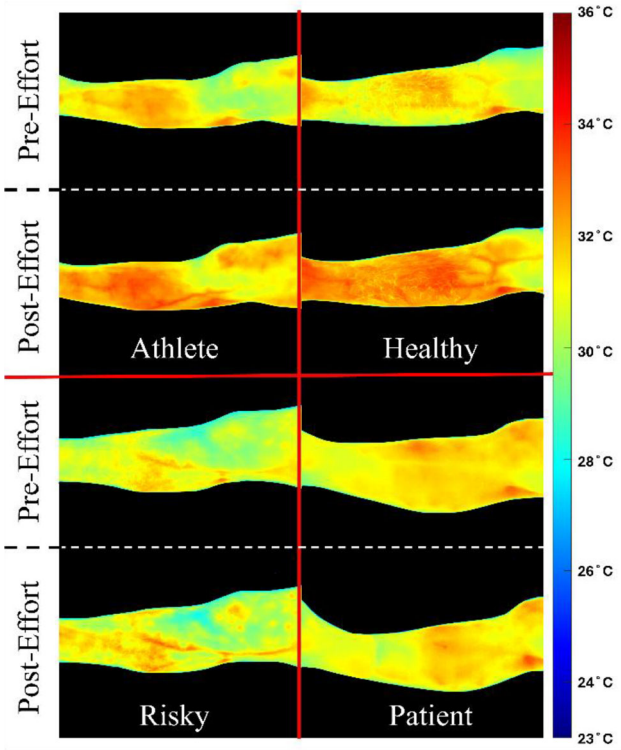


Fig. 11 Thermal images pre-effort and post-effort across all study groups

3 Results

Temperature variations in superficial tissue perfusion were analyzed across the athlete, healthy, at-risk, and patient groups. Effort-induced temperature responses differed noticeably between groups. The athlete group exhibited the greatest mean temperature increase (0.96 °C), reflecting enhanced vascular elasticity and superior microcirculatory capacity. Healthy individuals demonstrated a slightly lower average increase (0.79 °C) with relatively limited variability, indicating stable vascular function.

In contrast, the at-risk group showed a wider range of temperature changes (0.5–0.8 °C), suggesting inter-individual heterogeneity potentially associated with varying degrees of early microvascular dysfunction. The patient group exhibited the smallest temperature increase (0.38 °C), consistent with advanced vascular stiffness, impaired tissue perfusion, and markedly reduced adaptive capacity. The temperature responses observed for each group are presented in Fig. 9.

The mean tissue perfusion temperatures of the lower extremity peripheral vascular structures were evaluated for both pre- and post-effort conditions. Pre-effort temperatures were highly comparable across all groups, measuring 34.28 °C in the athlete group, 34.07 °C in the healthy group, 34.12 °C in the cardiovascular at-risk group, and 34.04 °C in the patient group. Following exertion, mean temperatures increased to 35.24 °C in the athlete group, 34.86 °C in the healthy group, 34.73 °C in the at-risk group, and 34.42 °C in the patient group. The pre- and post-exercise temperature values for all groups are illustrated in Fig. 10.

An analysis of pre- and post-effort temperatures revealed no statistically significant differences among the groups under resting conditions. Similarly, Huang et al. [22] reported no significant differences in baseline skin temperatures between patients and healthy individuals. In contrast, post-effort temperatures demonstrated clear intergroup differences. However, relying solely on post-effort temperature values may not sufficiently differentiate between the healthy and at-risk groups. Therefore, effort-induced temperature change (ΔT) appears to be a more discriminative parameter for group classification.

Representative infrared thermal images acquired before and after standardized physical exercise for all four study groups are presented in Fig. 11. For each group, pre-exercise and post-exercise images are displayed vertically for direct comparison. The color scale corresponds to absolute skin temperature values ranging from 23 to 36 °C. The athlete and healthy groups exhibit a pronounced post-effort temperature increase accompanied by spatial redistribution, reflecting efficient vasodilatory and microcirculatory responses. In contrast, the at-risk and patient groups show attenuated temperature elevation and more homogeneous thermal patterns,

consistent with impaired vascular reactivity associated with peripheral arterial disease and cardiovascular risk factors.

Haralick texture features are widely used in medical image analysis for assessing various diseases [36, 40]. The Haralick texture features extracted from the thermal data of the four different groups did not follow a normal distribution. Kruskal–Wallis H analysis revealed statistically significant differences in contrast ($p = 0.017 < 0.05$), and homogeneity ($p = 0.028 < 0.05$) among the extracted features (Table 2).

Statistically significant intergroup differences were observed in contrast ($p = 0.017$) and homogeneity ($p = 0.028$) ($p < 0.05$). The lower contrast and higher homogeneity values identified in the patient group suggest more uniform and less variable thermal patterns, likely attributable to peripheral vascular impairment. In contrast, the elevated contrast values observed in the athlete group indicate that regular physical activity may enhance peripheral blood circulation, resulting in more heterogeneous thermal distributions.

The energy, entropy, and correlation parameters did not demonstrate statistically significant differences between groups. Although the entropy value was lowest in the patient group—potentially reflecting reduced diversity in tissue thermal patterns associated with circulatory dysfunction—this difference did not reach statistical significance. Overall, these findings suggest that individuals with peripheral circulation disorders exhibit more homogeneous and low-contrast thermal characteristics, whereas athletes display more dynamic and heterogeneous thermal patterns.

Pairwise comparisons of the groups were also analyzed. The nonparametric Mann Whitney U test was used because the groups were not suitable for normal distribution. Pairwise comparisons of Haralick features using the Mann Whitney U test are presented in Table 3.

Contrast reflects local intensity variations within an image and highlights differences in spatial density distribution. The reduced blood flow in the lower extremities of the patient group, compared with the other groups, may account for the significant differences observed in pairwise comparisons. The significant difference identified between the at-risk and healthy groups may indicate early stage endothelial dysfunction in the at-risk group. Correlation describes the linear dependency between neighboring pixel intensities and reflects the consistency of thermal distribution. The athlete group demonstrated a more structured and spatially coherent heat distribution pattern. As this regularity was less pronounced in the at-risk and healthy groups, statistically significant differences between these groups and the athlete group were anticipated.

Energy quantifies textural uniformity and regularity within the image. Statistically significant differences were observed only in pairwise comparisons between the athlete and patient groups, suggesting higher textural regularity in athletes compared to patients. Entropy represents the degree of randomness or complexity within an image. A significant difference was observed only between the healthy and at-risk groups, which may be attributed to increased thermal irregularity associated with early endothelial dysfunction in the at-risk group. No significant differences were found between the athlete–risky or athlete–patient comparisons. This finding may reflect distinct underlying mechanisms: physiological vascular adaptation and increased vascular density in athletes, versus pathological vascular occlusion and perfusion impairment in patients.

Homogeneity indicates the similarity of neighboring pixel intensities and reflects the uniformity of thermal patterns. Superficial tissue perfusion in the lower extremities appeared more efficient in the athlete and healthy groups, whereas reduced perfusion was observed in the at-risk and patient groups, likely due to endothelial dysfunction and vascular stiffness. The significant differences identified between the at-risk group and both the athlete and patient groups support the interpretation of the at-risk group as an intermediate stage of disease progression. Among the Haralick texture features, homogeneity emerged as the most discriminative parameter for distinguishing between groups, demonstrating a consistent and clinically meaningful separation.

In this study, the dataset was partitioned into 70% for training, 15% for validation, and 15% for testing. Haralick texture features and frequency domain features were used as inputs to various classification algorithms, and the models achieving the highest performance were selected for further analysis. The primary objective was to classify the study groups based on these texture and frequency characteristics. Classification accuracy across the evaluated models ranged from 29.6 to 95.7%. The detailed performance results of the classifiers are summarized in Table 4.

According to the decision tree (DT) model results, the highest classification accuracy using Haralick features was achieved with the complex DT configuration (88.7%), whereas the application of principal component analysis (PCA) led to a reduction in performance. DT models demonstrated limited effectiveness in classifying frequency domain features. For the SVM models, the cubic SVM achieved the highest accuracy (95.7%) in the classification of Haralick features, while the complex Gaussian SVM also exhibited strong performance. In contrast, SVM performance on frequency features was moderate and did not reach a satisfactory level. Among the KNN models, the best performance for Haralick features was obtained with weighted KNN (94.8%) and quadratic KNN (94.5%). For frequency features, cosine KNN achieved an accuracy of 73.6%, which improved to 83.3% following the application of PCA. These findings indicate that PCA negatively affected classification performance when applied to Haralick texture features but had a positive impact when applied to frequency domain features.

Table 2 Results of the Kruskal–Wallis H test and median values of the groups

Group	Athlete	Healthy	Risky	Patient	*P* value
Contrast	0.079	0.068	0.050	0.032	0.017
Correlation	0.780	0.798	0.803	0.876	0.210
Energy	0.801	0.771	0.764	0.760	0.485
Homogeneity	0.979	0.968	0.963	0.962	0.028
Entropy	0.879	0.866	0.780	0.681	0.253

Table 3 Result of Mann–Whitney U test

Groups	Athlete-patient	Healthy-risky	Healthy-athlete	Athlete-patient	Athlete-risky	Risky-patient
Contrast	0.008	0.015	0.218	0.041	0.217	0.046
Correlation	0.659	0.829	0.022	0.267	0.033	0.319
Energy	0.079	0.215	0.180	0.043	0.536	0.219
Entropy	0.157	0.043	0.144	0.743	0.609	0.257
Homogeneity	0.035	0.183	0.539	0.003	0.038	0.030

Table 4 Accuracy of classification algorithms

Classifiers	Types	Haralick texture		Frequency	
		Features		Features	
		Without PCA (%)	With PCA (%)	Without PCA (%)	With PCA (%)
Decision tree (DT)	Complex	88.7	60.7	53.2	67.3
	Medium	85.2	61.6	53.2	62.4
	Basit	73.8	57.3	53.2	62.4
Support vector machines (SVM)	Linear	70.0	30.8	64.0	71.2
	Quadratic	90.3	29.6	64.5	71.2
	Cubic	**95.7**	32.9	63.1	62.7
	Complex Gauss	92.4	63.7	63.1	63.3
	Mean Gauss	86.3	59.4	62.7	63.3
K-nearest neighbor (K-NN)	Complete	94.1	58.0	55.0	62.0
	Medium	93.5	65.8	55.0	62.0
	Cosine	93.9	32.9	73.6	**83.3**
	Quadratic	94.5	67.0	55.0	57.6
	Weighted	94.8	58.4	63.4	57.6

Based on these results, cubic SVM algorithm was selected for the classification of Haralick texture features, while cosine KNN algorithm was chosen for frequency domain feature classification. In addition, hot-region distribution images were analyzed using a custom-designed CNN model. In total, three independent classification models were developed. Each model produced class probability (weight) coefficients for the four study groups. When a thermal image of an individual's lower extremity tissue perfusion was provided as input, a total of 12 weight coefficients were generated across the three models. To avoid manual integration of these outputs and to optimize final decision-making, the probability outputs of the three classifiers were used as input features for an XGB ensemble model.

Distinct trends were observed across several extracted features when comparing participant groups, particularly between patients with PAD and non-pathological cohorts. The patient group consistently demonstrated reduced contrast values, indicating decreased heterogeneity in thermal patterns and suggesting uniformly diminished peripheral perfusion. Likewise, elevated homogeneity values in this group

Table 5 Gain-based relative importance of feature groups contributing to the XGBoost ensemble classifier

Feature source	Feature description	Relative importance (%)
CNN	Hot region distribution	30
Haralick	Contrast	9
Haralick	Homogeneity	15
Haralick	Correlation	5
Haralick	Energy	18
Haralick	Entropy	7
Frequency	Dominant frequency	16

may reflect vascular stiffness and structural remodeling, as reduced arterial compliance can limit spatial temperature variability.

Frequency domain analysis revealed lower dominant frequency components in the patient group, corresponding to attenuated and delayed vasodilatory responses following physical exertion. This observation is consistent with established PAD-related impairments in microvascular reactivity and thermoregulatory adaptation. In contrast, CNN-derived hot-region distributions were more prominent in the athlete group, reflecting enhanced microcirculatory responsiveness and efficient vascular regulation. Collectively, these findings support the physiological plausibility of the extracted features and highlight their potential utility in distinguishing PAD-associated vascular dysfunction from healthy and high-performance circulatory profiles.

Gain-based feature importance analysis of the XGB meta-classifier is presented in Table 5. Among all feature sources, CNN-derived features representing hot-region distribution exhibited the highest relative contribution (30%) to the final classification decision. This finding indicates that spatial temperature patterns captured by the deep learning model play a dominant role in discriminating between vascular conditions. Haralick texture features collectively accounted for a substantial proportion of the decision process. Energy (18%) and homogeneity (15%) emerged as the most influential texture descriptors, followed by contrast (9%), entropy (7%), and correlation (5%). These results suggest that second-order texture statistics characterizing spatial uniformity and intensity distribution provide complementary discriminative information beyond CNN-derived representations. Frequency domain features also demonstrated meaningful relevance, with dominant frequency components contributing 16% to the overall model gain. This underscores the importance of frequency characteristics of thermal signals in capturing vascular response heterogeneity across participant groups. It should be noted that the reported feature importance values correspond to the relative contribution of class-wise probability outputs from the base classifiers to the XGB meta-classifier, rather than direct importance at the raw feature or pixel level.

The XGB model was trained using total of 240 augmented data samples. The training success rate of the XGB was 92.9%, the validation success rate was 93.4%, and the test success rate was 93.1%. The overall accuracy of the XGB model was calculated to be 93%. The confusion matrix and ROC curves obtained as a result of training the XGB model are shown in Fig. 12.

Analysis of the confusion matrix indicates that the XGB model effectively classified the four study groups, achieving an overall accuracy of 92.9%. Nevertheless, a certain degree of misclassification was observed for the at-risk group, primarily in relation to the healthy and patient classes. This overlap may be attributed to the intermediate thermal response characteristics of the at-risk group, which share features with both non-pathological and pathological profiles. In contrast, the athlete, healthy, and patient groups were classified with higher consistency, reflecting more distinct thermal and vascular response patterns. Receiver operating characteristic (ROC) curve analysis further demonstrated the discriminative capability of the model. The area under the curve (AUC) values were notably high for the athlete, healthy, and patient groups, indicating strong class separability. However, the at-risk group exhibited comparatively lower AUC values, likely reflecting its heterogeneous physiological characteristics and its transitional position between healthy and diseased states.

The classification performance of the proposed XGB-based ensemble model and confidence interval (CI) of performance metrics are summarized in Table 6. Based on the confusion matrix analysis, the model achieved an overall accuracy of 92.92%. Sensitivity, specificity, precision, and F1-score were computed using a one-vs-rest strategy and macro-averaged across the four classes (healthy, athlete, risky, and patient). The model yielded a macro-average sensitivity of 92.92%, a macro-average specificity of 97.36%, a macro-average precision of 92.93%, and a macro-average F1-score of 92.92%, indicating balanced classification performance across all participant groups.

ROC analysis supports the discriminative ability of the proposed framework. One-vs-rest ROC curves were generated using class probability outputs, and the AUC was computed separately for each class. The AUC value reflects that an acceptable distinction can be made between the four study groups. Collectively, these results demonstrate that the proposed approach achieves robust and well-balanced multi-class classification performance, supporting its potential applicability in functional vascular assessment.

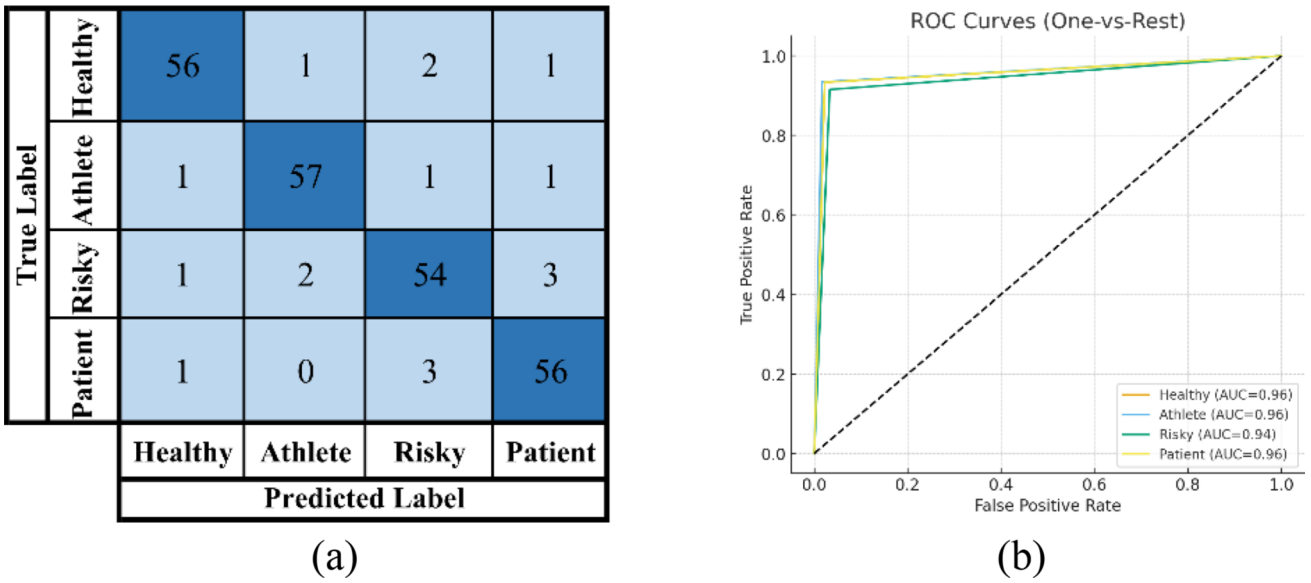


Fig. 12 **a** Confusion matrix of predicted label; **b** ROC curve of model

Table 6 Performance metrics of the proposed XGBoost-based ensemble model

Metric	Value	CI
Accuracy (%)	92.92	88.10–97.30
Sensitivity (%) (macro-average)	92.92	85.10–97.60
Specificity (%) (macro-average)	97.36	95.30–98.70
Precision (%) (macro-average)	92.93	89.50–95.40
F1-score (%) (macro-average)	92.92	87.80–97.10
AUC (macro-average)	0.96	0.91–0.99

To provide a more reliable assessment of the uncertainty associated with model performance metrics, 95% confidence intervals were calculated using the bootstrap resampling method. In this approach, 1000 bootstrap samples were generated from the test dataset using sampling with replacement, and for each iteration, accuracy, sensitivity, specificity, precision, F1-score, and AUC were recalculated. The 95% confidence intervals were determined by extracting the 2.5th and 97.5th percentiles from the resulting metric distributions. This approach is particularly suitable for studies with limited sample sizes, as it provides a more realistic estimation of the variability in performance metrics.

When examining the performance metrics and corresponding 95% confidence intervals of the XGB-based ensemble model, the overall accuracy was found to be 92.92%, with a confidence interval ranging from 88.10 to 97.30%. Similarly, the macro-average sensitivity and F1-score were both 92.92%, with relatively narrow confidence intervals, indicating stable performance across bootstrap samples. Notably, the specificity reached a high value of 97.36%, with a confidence interval of 95.30%–98.70%, demonstrating that the model is particularly consistent and reliable in distinguishing negative cases. The AUC value of 0.96 (0.91–0.99) further supports the model's strong discriminative capability and statistical robustness across classes. Overall, the relatively narrow confidence intervals suggest that the model's performance remains stable across bootstrap resampling iterations and does not exhibit substantial variability.

4 Discussion

This study proposes a new assistant medical diagnostic method that provides a completely non-invasive and reliable assessment of endothelial cell function, fibrosis-induced loss of elasticity, and cholesterol plaque formation in lower extremity peripheral vascular structures. The method classifies temperature variations in the superficial tissue perfusions of these structures across four groups, using a combination of Haralick texture features, homogeneity of temperature distribution, and frequency features (Fig. 1). Previous studies have evaluated peripheral vascular disease using thermal imaging without artificial intelligence or image processing algorithms [19, 27, 41]. These studies typically focused on temperature differences between the resting superficial tissue perfusion of healthy individuals and patients diagnosed with peripheral vascular disease through clinical testing. In contrast, the present study evaluates dynamic temperature responses under exertion conditions across four distinct groups, including an intermediate at-risk cohort. By combining thermal imaging with quantitative image analysis and

machine learning algorithms, this framework offers a complementary, non-invasive tool that may support the early detection and monitoring of lower extremity PAD.

Non-invasive diagnostic approaches for PAD commonly include the ABI, Doppler ultrasonography, and duplex ultrasound. While ABI is simple and cost-effective, it mainly reflects macrovascular obstruction and may fail to detect early microvascular dysfunction. Doppler and duplex ultrasound provide detailed hemodynamic and structural information; however, their operator dependency and requirement for specialized equipment limit their scalability for routine screening. In contrast, the infrared thermal imaging framework proposed in this study enables contactless, rapid, and functional assessment of vascular reactivity under physiological stress conditions. By capturing spatial temperature distribution and microcirculatory response patterns, this approach may offer enhanced sensitivity to early functional impairments that precede structural vascular changes. Therefore, it has the potential to serve as an accessible adjunct diagnostic tool for early PAD risk stratification and monitoring.

Several studies have assessed peripheral vascular disease using thermal imaging, many of which have shown temperature differences between the lower extremities of patients and healthy individuals at rest, without utilizing artificial intelligence or image processing algorithms [22, 25, 28, 30]. These studies primarily measured the tissue temperature at specific points or averaged the temperature values across regions, without examining temperature distribution or changes due to effort. Gauci et al. developed a method to automatically extract 44 predefined anatomical regions from thermal images of the hands, soles, and legs to monitor PAD using image processing algorithms [23]. However, their study focused on reducing the time required to manually determine temperature distributions, without extracting features for further analysis. Kostadinov proposed a method to assess lower extremity peripheral vascular disease using artificial intelligence and thermal images, comparing different machine learning models to classify differences between patients in advanced stages of the disease and healthy individuals, without effort involved [24]. The study only investigated the classification of thermal images belonging to patient and healthy individuals. Huang, demonstrated differences in temperature changes in the lower extremities of patients and healthy individuals due to effort [22]. The temperature changes resulting from exertion are thought to provide functional insights into the lower extremity peripheral vascular structures. Based on these results, the proposed diagnostic method in our study is expected to aid in the early diagnosis of the disease and help organize treatment plans more effectively.

In the thermal imaging protocol, the patella and ankle were used as standardized anatomical landmarks for all participants to ensure spatial consistency across recordings. To minimize motion artifacts during data acquisition, participants' feet were secured within a positioning apparatus extending to the ankle level. The use of anatomical landmarks is well established in thermal imaging research to enhance reproducibility and measurement accuracy [42]. During the normalization stage, cubic spline interpolation was employed to model the lower extremity regions. This method was selected due to its capability to generate smooth transitions in temperature gradients across adjacent pixels while preserving spatial continuity. Post-interpolation temperature gradients were analyzed to evaluate the potential impact of the interpolation process on thermal distribution patterns. Validation analyses indicated that high-temperature regions were not artificially diffused or distorted during interpolation. Cubic spline interpolation is widely reported in the literature as an effective technique for maintaining image integrity while ensuring smooth pixel-level transitions [43].

The proposed system enables the evaluation of the structural function of the lower extremity regions based on temperature changes due to effort. Classification between athletes, healthy, at-risk, and patients was achieved using these temperature changes. However, it was observed that classification could not be made solely using temperature values from pre-effort states. Therefore, temperature changes resulting from effort were determined to be crucial for the classification process between groups.

It was hypothesized that effort-dependent changes in temperature homogenization and superficial tissue perfusion heterogeneity represent key discriminative parameters across the study groups. To characterize these variations, temperature distribution maps were generated using K-means clustering. Subsequent classification modeling and statistical analyses confirmed significant intergroup differences. These findings indicate that the proposed system can effectively capture thermal patterns associated with alterations in vascular function, including reduced arterial compliance, perfusion abnormalities, and impaired vasodilatory responses. While the method does not directly measure structural changes such as plaque formation or complete intravascular flow loss, the observed thermal signatures may reflect underlying physiological processes related to these conditions across the four groups.

Statistical analysis of the Haralick texture features revealed significant intergroup differences ($p < 0.05$), particularly in contrast ($p = 0.017$) and homogeneity ($p = 0.028$) across the four study groups. These features were extracted from normalized difference images obtained between pre- and post-effort conditions. The findings indicate that both the magnitude of temperature change and the spatial distribution of these changes vary across groups. The study

included a total of 40 participants, evenly distributed among four groups. Although the sample size is relatively limited due to the feasibility nature of the study, the balanced group allocation ensured equitable representation for statistical comparisons and machine learning model development. Balanced class distribution is essential for minimizing bias and improving model generalizability. Group comparisons were performed using the Kruskal–Wallis H test, followed by Bonferroni-adjusted post hoc analyses to account for multiple comparisons, thereby enhancing the robustness of the statistical inferences. The overall effectiveness of the proposed approach is supported by the statistically significant findings and the classification performance achieved by the machine learning models.

Haralick texture features enable the examination of local regions within the thermal images, revealing differences in temperature change distribution between the groups. The statistical analysis confirmed that the Haralick texture features are suitable for modeling with classification algorithms. The cubic-type SVM algorithm, trained with Haralick texture features without PCA, achieved an accuracy of 95.7% during the testing phase. Frequency features were trained using the cosine-type KNN algorithm with PCA, resulting in an accuracy of 83.3% in the testing phase. Temperature distribution images were processed with CNN model, which also achieved an accuracy of 95.7%. These machine learning models effectively classify small datasets, with SVM and KNN performing well on limited data.

The gain-based importance analysis provides insight into the relative contributions of different feature sources within the proposed ensemble framework. The predominance of CNN-derived hot region distribution features suggests that macroscopic spatial temperature organization, likely influenced by perfusion heterogeneity and localized thermal gradients, is a key indicator of vascular dysfunction. The significant contribution of Haralick energy and homogeneity features aligns with known PAD-related alterations in microcirculatory regulation, where impaired blood flow leads to more heterogeneous and less uniform thermal distributions. Similarly, the relevance of dominant frequency features may reflect delayed or attenuated thermoregulatory responses to physiological stress, which have been associated with compromised arterial compliance. Overall, these findings support the hypothesis that combining deep spatial representations with handcrafted texture and frequency domain descriptors enables a more comprehensive characterization of PAD-related thermal signatures.

Although ABI is the current clinical standard for PAD assessment, a direct quantitative comparison between ABI and the proposed thermal imaging–based metrics was not performed in this study. This represents a limitation of the current work. However, ABI primarily reflects macrovascular obstruction, whereas thermal imaging captures functional microcirculatory and endothelial responses, particularly under physiological stress. Therefore, the proposed method is considered complementary rather than a replacement for ABI.

Although the reported classification accuracy is high, the relatively small sample size may raise concerns regarding potential overfitting. To address this issue, several precautionary measures were implemented. First, all dataset partitions were performed at the participant level, ensuring that no samples derived from the same individual—whether original or augmented—were distributed across the training, validation, and test sets. Second, data augmentation was applied exclusively to the training set to prevent information leakage. Third, the close agreement among training, validation, and test performance metrics suggests that the models captured generalizable patterns rather than memorizing subject-specific characteristics. Nevertheless, the findings should be interpreted within the context of a feasibility study, and further validation using larger, independent cohorts is necessary to confirm generalizability. The equal distribution of participants across four physiologically distinct groups ensured balanced class representation, which is essential for both robust statistical analysis and reliable machine learning model development. Moreover, the statistically significant differences identified in contrast and homogeneity features—despite the limited cohort size—suggest that the observed effect sizes are sufficiently pronounced to be detected under the current experimental framework.

Several limitations should be considered when interpreting the findings of this study. First, the relatively small sample size may limit statistical power and the generalizability of the results. Although participant-level data splitting and cross-validation were employed to reduce overfitting, the risk of model optimism cannot be completely eliminated. Second, the absence of direct comparison with gold-standard diagnostic methods such as the ABI or duplex ultrasound limits the ability to draw definitive clinical conclusions. Finally, despite controlled environmental conditions, thermal imaging measurements may be influenced by individual physiological variability, skin characteristics, or subtle differences in positioning.

In conclusion, the framework investigated in this study demonstrates potential as a non-invasive, computer-assisted approach for the detection and monitoring of peripheral vascular dysfunction. The proposed methodology may contribute to the evaluation of conditions such as peripheral atherosclerotic and non-atherosclerotic vascular diseases, diabetic vasculopathy, vasculitis, and other peripheral circulatory disorders. Beyond identifying established pathology,

the approach may also offer sensitivity to early endothelial dysfunction before overt clinical manifestations become apparent.

The findings indicate that thermal imaging combined with machine learning techniques can effectively differentiate PAD patients from healthy, at-risk, and athlete groups. Although several extracted features appear to be associated with vascular elasticity, perfusion abnormalities, and endothelial dysfunction, these associations should be interpreted cautiously, as further physiological and clinical validation is required. Accordingly, the proposed pathophysiological interpretations are presented as hypothesis-generating rather than definitive conclusions. While environmental conditions and exercise protocols were standardized, additional studies are necessary to evaluate the robustness and reproducibility of the method under diverse clinical and environmental settings.

Early detection and timely management of peripheral vascular disorders are critical for preventing long-term complications. As a fully non-invasive and relatively low-cost technique, the proposed framework has potential for broader clinical application, subject to further validation. In addition to peripheral vascular assessment, this approach may have translational relevance in other perfusion-related clinical contexts, such as intraoperative tissue viability evaluation, post–cold ischemia assessment of donor organs in transplantation, and monitoring of tissue flap perfusion.

Funding Open access funding provided by the Scientific and Technological Research Council of Türkiye (TÜBİTAK).

Declarations

Conflict of interest The authors of this manuscript declare no other conflict of interest.

Ethical approval This study was approved by the Research Ethics Committee of Akdeniz University Hospital (ethics committee approval number: 2012-KAEK-20) and a waiver of approval was given.

Open Access This article is licensed under a Creative Commons Attribution 4.0 International License, which permits use, sharing, adaptation, distribution and reproduction in any medium or format, as long as you give appropriate credit to the original author(s) and the source, provide a link to the Creative Commons licence, and indicate if changes were made. The images or other third party material in this article are included in the article's Creative Commons licence, unless indicated otherwise in a credit line to the material. If material is not included in the article's Creative Commons licence and your intended use is not permitted by statutory regulation or exceeds the permitted use, you will need to obtain permission directly from the copyright holder. To view a copy of this licence, visit http://creativecommons.org/licenses/by/4.0/.

References

1. Joosten, M.M.; Pai, J.K.; Bertoia, M.L.; Rimm, E.B.; Spiegelman, D.; Mittleman, M.A.; Mukamal, K.J.: Associations between conventional cardiovascular risk factors and risk of peripheral artery disease in men. JAMA **308**, 1660–1667 (2012). https://doi.org/10.1001/jama.2012.13415
2. Norgren, L.; Hiatt, W.R.; Dormandy, J.A.; Nehler, M.R.; Harris, K.A.; Fowkes, F.G.R.: Inter-society consensus for the management of peripheral arterial disease (TASC II). TASC **II**(45), S5–S67 (2007). https://doi.org/10.1016/j.jvs.2006.12.037
3. Peltokangas, M.; Vakhitov, D.; Suominen, V.; Korhonen, J.; Huotari, M.; Verho, J.; Röning, J.; Mattila, V.M.; Romsi, P.; Oksala, N.; Vehkaoja, A.: Lower limb pulse rise time as a marker of peripheral arterial disease. IEEE Trans. Biomed. Eng. **66**, 2596–2603 (2019). https://doi.org/10.1109/TBME.2019.2892407
4. Hiatt, W.R.: Medical treatment of peripheral arterial disease and claudication. N. Engl. J. Med. **344**, 1608–1621 (2001). https://doi.org/10.1056/NEJM200105243442108
5. Price, J.F.; Mowbray, P.I.; Lee, A.J.; Rumley, A.; Lowe, G.D.O.; Fowkes, F.G.R.: Relationship between smoking and cardiovascular risk factors in the development of peripheral arterial disease and coronary artery disease; Edinburgh Artery Study: Edinburgh Artery Study. Eur. Heart J. **20**, 344–353 (1999). https://doi.org/10.1053/euhj.1998.1194
6. Dua, A.; Lee, C.J.: Epidemiology of peripheral arterial disease and critical limb ischemia. Tech. Vasc. Interv. Radiol. **19**, 91–95 (2016). https://doi.org/10.1053/j.tvir.2016.04.001
7. Qin, Y.; Wu, J.; Hu, Q.; Ghista, D.N.; Wong, K.K.: Computational evaluation of smoothed particle hydrodynamics for implementing blood flow modelling through CT reconstructed arteries. J. X-Ray Sci. Technol. **25**, 213–232 (2017)
8. Mc Dermott, M.M.; Greenland, P.; Guralnik, J.M.; Liu, K.; Criqui, M.H.; Pearce, W.H.; Chan, C.; Schneider, J.; Sharma, L.; Taylor, L.M.; Arseven, A.; Quann, M.; Celic, L.: Depressive symptoms and lower extremity functioning in men and women with peripheral arterial disease. J. Gen. Intern. Med. **18**, 461–467 (2003). https://doi.org/10.1046/j.1525-1497.2003.20527.x
9. Bettmann, M.A.; Heeren, T.; Greenfield, A.; Goudey, C.: Adverse events with radiographic contrast agents: results of the SCVIR Contrast Agent Registry. Radiology **203**, 611–620 (1997). https://doi.org/10.1148/radiology.203.3.9169677
10. Xu, D.; Li, J.; Zou, L.; Xu, Y.; Hu, D.; Pagoto, S.L.; Ma, Y.: Sensitivity and specificity of the ankle—brachial index to diagnose peripheral artery disease: a structured review. Vasc. Med. **15**, 361–369 (2010). https://doi.org/10.1177/1358863X10378376
11. Olin, J.W.; Sealove, B.A.: Peripheral artery disease: current insight into the disease and its diagnosis and management. Mayo Clin. Proc. **85**, 678–692 (2010). https://doi.org/10.4065/mcp.2010.0133
12. Vlachopoulos, C.; Georgakopoulos, C.; Koutagiar, I.; Tousoulis, D.: Diagnostic modalities in peripheral artery disease. Cardiovasc. Ren. **39**, 68–76 (2018). https://doi.org/10.1016/j.coph.2018.02.010
13. Shin, T.; Menon, R.G.; Thomas, R.B.; Cavallo, A.U.; Sarkar, R.; Crawford, R.S.; Rajagopalan, S.: Unenhanced velocity-selective MR angiography (VS-MRA): initial clinical evaluation in patients with peripheral artery disease. J. Magn. Reson. Imaging **49**, 744–751 (2019). https://doi.org/10.1002/jmri.26268
14. Bhaduri, J.; Raisuddin, M.; Sarmin, M.; Sayeed, M.; Islam, M.: Prevalence and pattern of lower limbs peripheral artery disease detected by Duplex ultrasonography in patients having coronary artery blockage. TAJ J. Teach. Assoc. **29**, 62–65 (2016)
15. Moyer, V.A.: Screening for peripheral artery disease and cardiovascular disease risk assessment with the ankle–brachial index in

adults: U.S. Preventive Services Task Force recommendation statement. Ann. Intern. Med. **159**, 342–348 (2013). https://doi.org/10.7326/0003-4819-159-5-201309030-00008
16. Carlak, H.F.; Gencer, N.G.; Besikci, C.: Theoretical assessment of electro-thermal imaging: a new technique for medical diagnosis. Infrared Phys. Technol. **76**, 227–234 (2016). https://doi.org/10.1016/j.infrared.2016.03.001
17. Ring, E.; Ammer, K.: Infrared thermal imaging in medicine. Physiol. Meas. **33**, R33 (2012)
18. Lahiri, B.B.; Bagavathiappan, S.; Jayakumar, T.; Philip, J.: Medical applications of infrared thermography: a review. Infrared Phys. Technol. **55**, 221–235 (2012). https://doi.org/10.1016/j.infrared.2012.03.007
19. Bagavathiappan, S.; Saravanan, T.; Philip, J.; Jayakumar, T.; Raj, B.; Karunanithi, R.; Panicker, T.; Korath, M.P.; Jagadeesan, K.: Infrared thermal imaging for detection of peripheral vascular disorders. J. Med. Phys. **34**, 43 (2009)
20. Staffa, E.; Bernard, V.; Kubicek, L.; Vlachovsky, R.; Vlk, D.; Mornstein, V.; Bourek, A.; Staffa, R.: Infrared thermography as option for evaluating the treatment effect of percutaneous transluminal angioplasty by patients with peripheral arterial disease. Vascular **25**, 42–49 (2017)
21. Wallace, G.A.; Singh, N.; Quiroga, E.; Tran, N.T.: The use of smart phone thermal imaging for assessment of peripheral perfusion in vascular patients. Ann. Vasc. Surg. **47**, 157–161 (2018). https://doi.org/10.1016/j.avsg.2017.07.028
22. Huang, C.-L.; Wu, Y.-W.; Hwang, C.-L.; Jong, Y.-S.; Chao, C.-L.; Chen, W.-J.; Wu, Y.-T.; Yang, W.-S.: The application of infrared thermography in evaluation of patients at high risk for lower extremity peripheral arterial disease. J. Vasc. Surg. **54**, 1074–1080 (2011). https://doi.org/10.1016/j.jvs.2011.03.287
23. Gauci, J.; Falzon, O.; Formosa, C.; Gatt, A.; Ellul, C.; Mizzi, S.; Mizzi, A.; Sturgeon Delia, C.; Cassar, K.; Chockalingam, N.: Automated region extraction from thermal images for peripheral vascular disease monitoring. J. Healthc. Eng. **2018**(1), 5092064 (2018)
24. Kostadinov, G.: AI-enabled infrared thermography: machine learning approaches in detecting peripheral arterial disease. In: Zlateva, T.; Tuparov, G. (Eds.) Computer science and education in computer science, pp. 159–170. Springer Nature Switzerland, Cham (2023)
25. Sowa, M.; Friesen, J.; Hain, M.: Evaluating the potential of infrared thermography in the study of peripheral arterial occlusive disease. Meas. **7**, 427 (2009)
26. Deng, F.; Tang, Q.; Zeng, G.; Wu, H.; Zhang, N.; Zhong, N.: Effectiveness of digital infrared thermal imaging in detecting lower extremity deep venous thrombosis. Med. Phys. **42**, 2242–2248 (2015). https://doi.org/10.1118/1.4907969
27. de Carvalho Abreu, A.J.; de Oliveira, R.A.; Martin, A.A.: Correlation between ankle-brachial index and thermography measurements in patients with peripheral arterial disease. Vascular **30**, 88–96 (2022). https://doi.org/10.1177/1708538121996573
28. Kleiss, S.F.; Ma, K.F.; El Moumni, M.; Ünlü, Ç.; Nijboer, T.S.; Schuurmann, R.C.L.; Bokkers, R.P.H.; de Vries, J.-P.P.M.: Detecting changes in tissue perfusion with hyperspectral imaging and thermal imaging following endovascular treatment for peripheral arterial disease. J. Endovasc. Ther. **30**, 382–392 (2023). https://doi.org/10.1177/15266028221082013
29. Zbroja, H.; Kowalski, M.; Lubkowska, A.: The effect of dry carbon dioxide bathing on peripheral blood circulation measured by thermal imaging among patients with risk factors of PAD. Int. J. Environ. Res. Public Health (2021). https://doi.org/10.3390/ijerph18041490
30. Zenunaj, G.; Lamberti, N.; Manfredini, F.; Traina, L.; Acciarri, P.; Bisogno, F.; Scian, S.; Serra, R.; Abatangelo, G.; Gasbarro, V.: Infrared thermography as a diagnostic tool for the assessment of patients with symptomatic peripheral arterial disease undergoing infrafemoral endovascular revascularisations. Diagnostics (2021). https://doi.org/10.3390/diagnostics11091701
31. Kass, M.; Witkin, A.; Terzopoulos, D.: Snakes: active contour models. Int. J. Comput. Vision **1**, 321–331 (1988)
32. Wu, W.-C.; Wang, T.-H.; Chiu, C.-T.: Edge curve scaling and smoothing with cubic spline interpolation for image up-scaling. J. Signal Process. Syst. **78**, 95–113 (2015). https://doi.org/10.1007/s11265-014-0936-6
33. EtehadTavakol, M.; Sadri, S.; Ng, E.Y.K.: Application of K- and Fuzzy c-Means for color segmentation of thermal infrared breast images. J. Med. Syst. **34**, 35–42 (2010). https://doi.org/10.1007/s10916-008-9213-1
34. Gao, F.; Wu, T.; Li, J.; Zheng, B.; Ruan, L.; Shang, D.; Patel, B.: SD-CNN: a shallow-deep CNN for improved breast cancer diagnosis. Comput. Med. Imaging Graph. **70**, 53–62 (2018). https://doi.org/10.1016/j.compmedimag.2018.09.004
35. Xiao, Z.; Su, Y.; Deng, Z.; Zhang, W.: Efficient combination of CNN and transformer for dual-teacher uncertainty-guided semi-supervised medical image segmentation. Comput. Methods Programs Biomed. **226**, 107099 (2022). https://doi.org/10.1016/j.cmpb.2022.107099
36. Hapsari, R.K.; Miswanto, M.; Rulaningtyas, R.; Suprajitno, H.; Seng, G.H.: Modified gray-level Haralick texture features for early detection of Diabetes Mellitus and high cholesterol with iris image. Int. J. Biomed. Imaging **2022**, 5336373 (2022). https://doi.org/10.1155/2022/5336373
37. Anderson, D.R.; Burnham, K.P.; Thompson, W.L.: Null hypothesis testing: problems, prevalence, and an alternative. J. Wildl. Manage. (2000). https://doi.org/10.2307/3803199
38. Al Shibli, M.; Marques, P.: Artificial intelligent nonlinear autoregressive external input neural network modeling, design and control of a sea wave electro-mechanical power generating system. Int. J. Intell. Syst. Appl **9**, 1 (2019)
39. Fanfani, M.; Marulli, M.; Nesi, P.: Evaluation of geometric and photometric data augmentation for pedestrian detection with thermal cameras. Presented at the International Conference on Computational Science and Its Applications (2024)
40. Azevedo Tosta, T.A.; de Faria, P.R.; Neves, L.A.; do Nascimento, M.Z.: Evaluation of statistical and Haralick texture features for lymphoma histological images classification. Comput. Methods Biomech. Biomed. Eng. Imaging Vis. **9**, 613–624 (2021). https://doi.org/10.1080/21681163.2021.1902401
41. Shabani Varaki, E.; Gargiulo, G.D.; Penkala, S.; Breen, P.P.: Peripheral vascular disease assessment in the lower limb: a review of current and emerging non-invasive diagnostic methods. Biomed. Eng. OnLine **17**, 61 (2018). https://doi.org/10.1186/s12938-018-0494-4
42. Hildebrandt, C.; Raschner, C.; Ammer, K.: An overview of recent application of medical infrared thermography in sports medicine in Austria. Sensors **10**, 4700–4715 (2010)
43. Meijering, E.H.: Spline interpolation in medical imaging: comparison with other convolution-based approaches. Presented at the 2000 10th European Signal Processing Conference (2000)